

Received 20 July 2015

Accepted 9 October 2015

Edited by V. Favre-Nicolin, CEA and Université Joseph Fourier, France

Keywords: polarization; scattering; RSoXS; PSoXS; resonant scattering; simulation.

Origins of polarization-dependent anisotropic X-ray scattering from organic thin films

Eliot Gann,^{a,b} Brian A. Collins,^c Maolong Tang,^b John R. Tumbleston,^b Subrangs Mukherjee^b and Harald Ade^{b*}

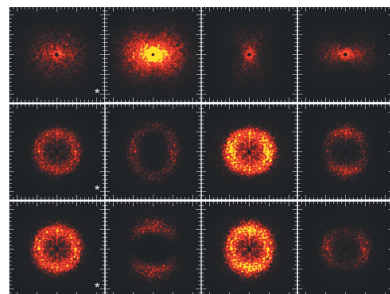
^aAustralian Synchrotron, 800 Blackburn Road, Clayton, Victoria 3168, Australia, ^bDepartment of Physics, NCSU, Raleigh, NC 27695-8202, USA, and ^cMaterials Science and Engineering Division, NIST, Gaithersburg, MD 20899-1070, USA.

*Correspondence e-mail: harald_ade@ncsu.edu

Organic thin films that have no overall in-plane directional ordering often nonetheless produce anisotropic scattering patterns that rotate with the polarization of incident resonant X-rays. Isotropic symmetry is broken by local correlations between molecular orientation and domain structure. Such examples of molecular alignment at domain interfaces and within the bulk of domains, which are both critical to fields such as organic electronics, are simulated and compared with experimental scattering. Anisotropic scattering patterns are found to allow unambiguous identification of the mechanism of local molecular orientation correlations and, as such, promise to be both distinct and complementary to isotropic scattering intensity as a general measure of thin film microstructure.

1. Introduction

Films made without overall directional bias can produce anisotropic scattering patterns (ASPs) when probed by linearly polarized resonant (*i.e.* at an absorption edge) X-rays (Collins *et al.*, 2012; Ma *et al.*, 2013; Gann *et al.*, 2012; Albrecht *et al.*, 2014; Li *et al.*, 2014; Liu *et al.*, 2013). This polarization-dependent anisotropic X-ray scattering (PAXS) is fundamentally different from ASPs that correlate with sample orientation in films created by a directional application or processing technique such as stretching (Ma *et al.*, 2015). In contrast, PAXS, observed first by Collins *et al.* (2012), is unaffected upon rotation of the sample, rotating rather with the polarization of incident resonant X-rays. In this initial work, the scattering patterns appeared to show highly vertically aligned ~ 300 nm domain structure when probed by horizontal polarized X-rays, but highly horizontal domain structures when the incident X-ray polarization was changed to vertical. It was proposed that interface-nucleated molecular alignment between domains could be the source of asymmetry (Collins *et al.*, 2012). Such interfacial alignment would be important to fundamental electronic device processes including charge separation and recombination which occur across interfaces (Sirringhaus *et al.*, 2000). An alternative mechanism proposed by Liu *et al.* (2013) is homogeneously nucleated bulk alignment, in the form of elongated crystalline fibrils, where one component forms a disordered network of elongated crystals, each grown along a single crystalline axis (fibrils), while the remainder of the film is isotropic and fills the voids between the fibrils (Liu *et al.*, 2013; Tang & McNeill, 2013; Savenije *et al.*, 2006). Bulk molecular alignment as in fibrils could be important to both geminate recombination and



© 2016 International Union of Crystallography

charge transport in organic electronics. Further investigations have revealed PAXS to correlate well with optoelectronic properties (Tumbleston *et al.*, 2014), but the source of the PAXS, *i.e.* the specific way in which molecular orientation–composition correlations (MOCCs) occur within the film, has not been established. We would like to emphasize here that conceptually it is the correlation between local molecular alignment and compositional changes which breaks the symmetry necessary to produce PAXS. Recently, there has been further confusion in the field with the suggestion than symmetric domains with uniform alignment within domains but random alignment between domains can produce PAXS (Diao *et al.*, 2015), clearly showing the importance of further conceptual development and quantification of PAXS. Molecular alignment by itself, uncorrelated to a domain boundary, and, *vice versa*, domain structures uncorrelated to local molecular alignment, do not break isotropic symmetry, and so cannot produce PAXS. While real systems likely exhibit a combination of bulk and interfacial alignment, identifying the unique PAXS signatures that arise from these alignment mechanisms can unlock a novel quantitative measure of film microstructure and allow a detailed understanding of the underlying physics of self-assembly.

We simulate PAXS at the carbon 1s absorption edge from different MOCCs, to develop criteria to distinguish these ordering paradigms and to explore microstructural details only undiscernible with resonant, polarized probes. We additionally explore how PAXS circumvents Babinet's principle: that scattering, sensitive only to composition, cannot determine which material is the matrix or dispersion in a binary system (Born & Wolf, 1980).

Organic molecules are often locally anisotropic both in their self-organization and resonant X-ray spectroscopic properties. This anisotropy originates from conjugated molecular ring structures that create a uniaxial symmetry orthogonal to the ring and characterized by the carbon C 1s $\rightarrow \pi^*$ transition dipole moment (TDM) (Wang *et al.*, 2011; O'Connor *et al.*, 2011). Molecules commonly stack along this direction, in $\pi-\pi$ stacking, both in liquid-crystalline domains and in extended fibril structures. Molecular alignment is ‘face-on’ when the TDM is orthogonal to an interface and ‘edge-on’ if the TDM is parallel. Thus the interfaces of fibrils formed by $\pi-\pi$ stacking are largely edge-on to the surrounding medium, while interface-nucleated alignment can be in either orientation depending on whether the interfacial interaction is dominated by the aliphatic side-chains included for solubility purposes or the aromatic backbone. In this work, we simulate each of these scenarios. We

additionally compare experimental data for the case of a fibril structure.

We choose, for realistic arrangements of optical parameters, to match an experimental system, and, for conceptual simplicity, a single uniaxial material poly(3-hexylthiophene) (P3HT) and the isotropic material phenyl-C₆₁-butyric acid methyl ester (PCBM), which are widely used in organic photovoltaics (Brady *et al.*, 2011). The optical constants span a realistic range for all organic systems and are representative of many different systems at different X-ray energies. The specific anisotropic behaviors should be understood to result from the MOCC and the relative arrangement of refractive indices (Watts *et al.*, 2011). It may be noted here that our methodology applies equally to systems where multiple components have alignment, although in this work we consider only a single aligned material.

2. Methods

2.1. MOCC modeling

Our model coarse-grains the P3HT PCBM mixture onto a lattice of relative material composition and preferential molecular alignment. Each lattice point contains a scalar (Φ_i) representing the concentration of each material i and a vector (\vec{s}_i) representing the preferential statistical alignment of the transition dipole moments of that material. These are represented by the color and lines, respectively, in Fig. 1. The total composition $\Phi = \sum \Phi_i \cong 1$, meaning space is filled and Φ_i and $|\vec{s}_i|$ are constrained to be less than 1 and positive. \vec{s}_i is a

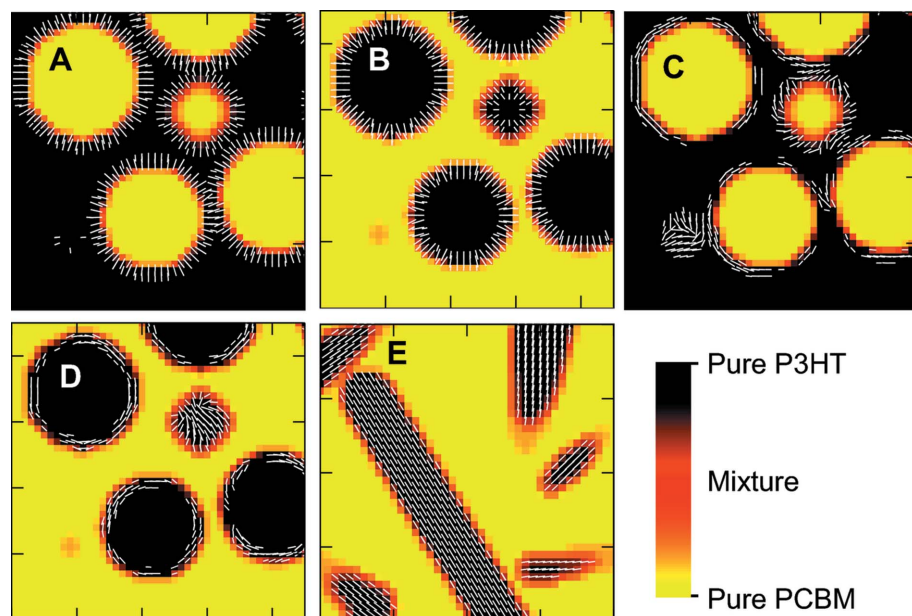


Figure 1

Close-up cross sections of modeled MOCCs. Cross sections shown are 200 nm \times 200 nm out of 2560 nm \times 2560 nm full simulation, taken in the middle of the film of simulated (a) interfacial alignment face-on to spherical dispersions, (b) face-on within spherical dispersions, (c) edge-on to spherical dispersions, (d) edge-on within spherical dispersions, and (e) bulk alignment within edge-on fibrils. Lines represent \vec{s} (which is only non-zero within the P3HT phase) projected onto the cross-sectional plane.

director field because of the point symmetry of the dipole moment, so that $\vec{s}_i \equiv -\vec{s}_i$. Morphology is completely determined by $\Phi_i(\vec{r})$. Alignment maps \vec{s}_i are calculated subsequently by a Monte Carlo algorithm in the case of interfacial alignment, but in the case of the fibril morphology both morphology and alignment are created in the same step.

We pick two representative morphologies in this study. Both are modeled in three dimensions, on a lattice with dimensions of $2560 \text{ nm} \times 2560 \text{ nm} \times 240 \text{ nm}$. The voxel size is 5 nm , meaning the number of lattice points is $512 \times 512 \times 48$ voxels. This simulation size is adequate to model the real resolution and coherence limit of soft X-ray scattering beamlines (Gann *et al.*, 2012) on realistically scaled thin films. X-rays are simulated with the incoming \vec{k} perpendicular to the thickness of the film, modeled on the usual arrangement for thin film P-SoXS experiments (Collins *et al.*, 2012).

First we create a three-dimensional system of random spherical dispersions by sequentially adding non-overlapping spheres, with radii chosen from a log normal distribution, to the three-dimensional system until $\sim 30\%$ volume fraction is achieved, depicted in Figs. 1(a)–1(d). The width of the log normal distribution of radii for spheres is 5 nm . To model fibrils (Fig. 1e), we assume that the fibril axis is along the π^* transition dipole moment of the polymers (Singh *et al.*, 2010; Kozub *et al.*, 2011). As only a portion of the material is known to crystallize, the matrix phase is consequently a mixture of amorphous polymers and fullerene (Collins *et al.*, 2010; Chen *et al.*, 2011; Collins, Li *et al.*, 2011; Collins, Tumbleston *et al.*, 2011; Gadisa *et al.*, 2012; He *et al.*, 2012). The system as a whole is constrained to have a 50% volume fraction of each material.

2.2. Calculating alignment density

In the matrix-dispersion morphology, a Monte Carlo method propagates alignment from the interfaces into the material. The spatial gradient of composition is used to determine the interfaces in the system. We define an energy cost to be differently aligned from this gradient, a cost to be differently aligned from nearest neighbors, and an entropic energy cost of having any preferential alignment. Starting from an initial grid of very small random preferential alignment vectors for all points in space, the algorithm calculates the total energy of the configuration. A metropolis test applied to each alignment location is utilized to evolve the system. The Monte Carlo proceeds through the system and, after approximately 200 steps per grid location, an energy minimum ($<10^{-3}$ percent change per step) can be reached. This results in a preferential alignment field $\vec{s}_i(\vec{r})$.

In the bulk-aligned fibril morphology, the alignment is determined during creation of each fibril. All alignment within the fibril is set to be along the long axis of the cylinder with unity magnitude. Close-up cross-sections of the resulting MOCCs are shown in Fig. 1.

The simulated MOCCs are designed to represent a single alignment paradigm with realistic levels of disorder and polydispersity, to be directly comparable with experimental scattering patterns, but comparison with experiment often

requires consideration of a combination of effects, including film thickness variations, isotropic scattering backgrounds and potentially any number of MOCCs.

2.3. Calculating optical constants and scattering contrasts from measurements

Experimental optical constants are available in existing databases (Watts *et al.*, 2011) and were calculated from absorption spectra by use of the Kramers–Kronig relations, explained in detail elsewhere (Watts, 2014; Yan *et al.*, 2013).

To obtain the theoretical perfectly aligned anisotropic optical constants, which cannot be experimentally collected for these largely disordered materials, it is necessary to extrapolate from experimentally collected spectra, as has been demonstrated elsewhere (Schuettfort *et al.*, 2012). First absorption spectra are collected when the polarization axis of the incident X-rays is at the ‘magic’ angle of 54.7° from the normal to a spin-cast thin film. This angle is where contributions between any in-plane or out-of-plane preferential alignments are balanced, so that the faces of the molecules are on average $1/3$ aligned with the electric field and $2/3$ unaligned. This measurement we take as a perfectly isotropic measure of the molecules absorption. This assumption is typically valid in spin-cast systems, where the only preferential direction is normal to the surface and so any macro-scale preferential alignment must be either along or perpendicular to this direction.

At normal incidence, the spectroscopic signal changes significantly, particularly at the P3HT carbon 1s to π^* TDM peak near an X-ray energy of 285 eV . Although we have no knowledge of the absolute fraction of face-on molecules that are aligned along the incident X-ray polarization vector at this orientation, all that is required is that we can quantify the difference between the normal-incidence signal and the unaligned signal. Using this difference, we linearly extrapolate from the isotropic spectra until the π^* peak is very close to zero (when $TDM \perp \vec{E}$). This linear extrapolation is valid in the case of uniaxial symmetry and roughly flat conjugation present in these conjugated systems (Pasquali *et al.*, 2008; Wang *et al.*, 2011).

This set of optical constants, with the π^* peak reduced to nearly zero, we call the perpendicular optical constant or perpendicular index of refraction (n_{\perp}). Comparing this extreme set of optical constants with the unaligned constants, we extrapolate back in the opposite direction twice the factor that was needed to remove the π^* peak, and obtain the 100% aligned optical constants which we call the parallel index of refraction (n_{\parallel}). All of these optical constants are shown in Fig. 2.

Having these optical constants for each material, we can calculate the respective binary contrasts $|\Delta n^2| = |\Delta\delta|^2 + |\Delta\beta|^2$ between each of the potential components in the thin film, shown in Fig. 2(b). Although not used in the simulation, they are useful in understanding the anisotropic scattering signals, because the scattering signal at a particular energy will be largely due to the contrast between materials which is domi-

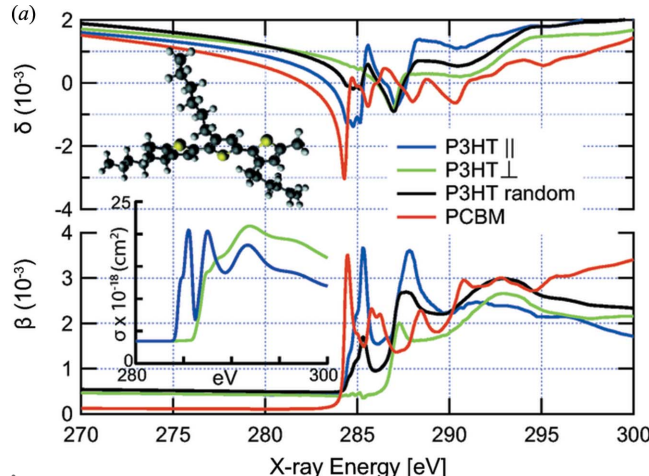


Figure 2

Optical constants and materials contrasts. (a) Optical constants. Top: the real deviation from 1 (δ). Bottom: the imaginary part (β) of the index of refraction ($n = 1 - \delta + i\beta$), measured and calculated at different angles relative to the polarization axis of incident X-rays. The inset is a calculation of parallel and perpendicular β for comparison and a drawing of the P3HT molecule. (b) Scattering contrasts calculated between different components in a P3HT PCBM film with molecular alignment of P3HT.

nant at that energy. For instance, at low and high energies, the orientational contrast between aligned phases of P3HT is low, while near 285 eV it is maximized.

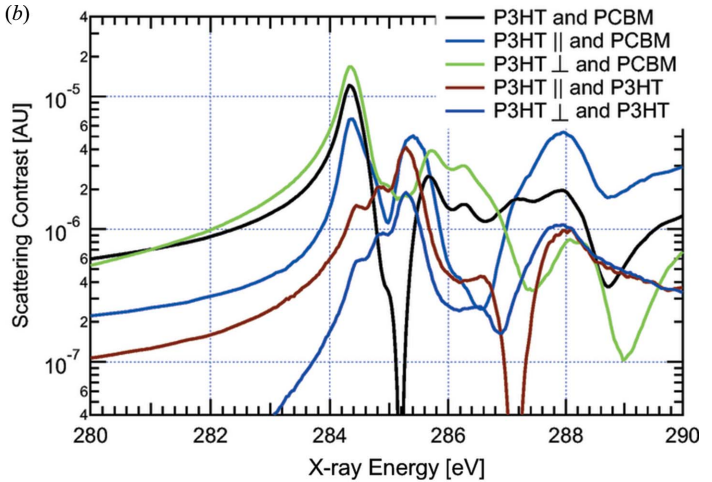
2.4. Calculating optical constants from DFT

We confirm the validity of these projected extreme optical constants by comparing them with simulated optical constants obtained by density functional theory (DFT), shown in the inset of Fig. 2(a). The equilibrium geometry for P3HT was determined by molecular dynamics using a universal force field (Goddard, 1992). The carbon 1s X-ray absorption spectra of the molecule were calculated by DFT using the computer code *StoBe* (Hermann *et al.*, 2007). For the purpose of our calculations, we used all-electron triple- ζ valence plus polarization (TZVP) atomic Gaussian basis sets for carbon and sulfur centers, while the hydrogen basis sets were chosen to be of the (311/1) type (Godbout *et al.*, 1992). To calculate X-ray absorption spectra, the Slater transition state method was applied (Slater, 1972). In this case the optimized geometry obtained from the geometric optimization calculation was kept fixed and incident X-ray polarization and angle-dependent absorption spectra were calculated. In order to obtain an improved representation of relaxation effects in the inner orbitals, the ionized center was described by using the IGLO-III basis (Huzinaga, 1965). A diffuse even-tempered augmentation basis set was finally included at the excitation center to account for transitions to unbound resonances. The absorption spectra were generated through a Gaussian convolution of the discrete spectra with varying broadenings.

2.5. Physical model of polarization-dependent scattering

We use the equation for induced molecular polarization \vec{p} in a material due to an external electric field

$$\vec{p} = \frac{(\hat{n}^2 - I) \cdot \vec{E}}{4\pi}, \quad (1)$$



where \hat{n} is the tensor index of refraction which, in the frame in which the uniaxial axis \vec{s} is unitary and aligned along \hat{x} , is diagonalized to

$$\hat{n}_x = \begin{pmatrix} n_{||} & 0 & 0 \\ 0 & n_{\perp} & 0 \\ 0 & 0 & n_{\perp} \end{pmatrix}. \quad (2)$$

These two energy-dependent complex numbers (the parallel $n_{||}$ and perpendicular n_{\perp} indices of refraction) are required for each material, as solved for in §2.3. At each lattice point, and in each material (i) \hat{n} is rotated and scaled according to \vec{s} , resulting in

$$\hat{n} = \frac{1}{|\vec{s}|} \times \begin{pmatrix} n_{||} s_x^2 + n_{\perp} s_y^2 + n_{\perp} s_z^2 & -(n_{\perp} - n_{||}) s_x s_y & -(n_{\perp} - n_{||}) s_x s_z \\ -(n_{\perp} - n_{||}) s_x s_y & n_{||} s_x^2 + n_{\perp} s_y^2 + n_{\perp} s_z^2 & -(n_{\perp} - n_{||}) s_y s_z \\ -(n_{\perp} - n_{||}) s_x s_z & -(n_{\perp} - n_{||}) s_y s_z & n_{||} s_x^2 + n_{\perp} s_y^2 + n_{\perp} s_z^2 \end{pmatrix} \quad (3)$$

where s_α are the Cartesian components of \vec{s} , not to be confused with \vec{s}_i which is the molecular alignment within material i . An additional unaligned portion, which has the average index of refraction $\langle \hat{n} \rangle^2 = (n_{||}^2 + 2n_{\perp}^2)/3$, is defined as $\Phi_{ui} = \Phi_i - |\vec{s}_i|$, such that in this model each material can have one preferential direction and otherwise random alignment. Setting the coordinate system, as shown in Fig. 3(A), such that the incoming X-ray polarization (E -field) is unitary along the z axis, $\vec{E} = \hat{z}$, we calculate the components of induced molecular polarization \vec{p} at each lattice point from equations (1) and (3), which are easiest to examine component by component, with p_z being in the excited direction, and so has components from both the aligned and unaligned portions of each material,

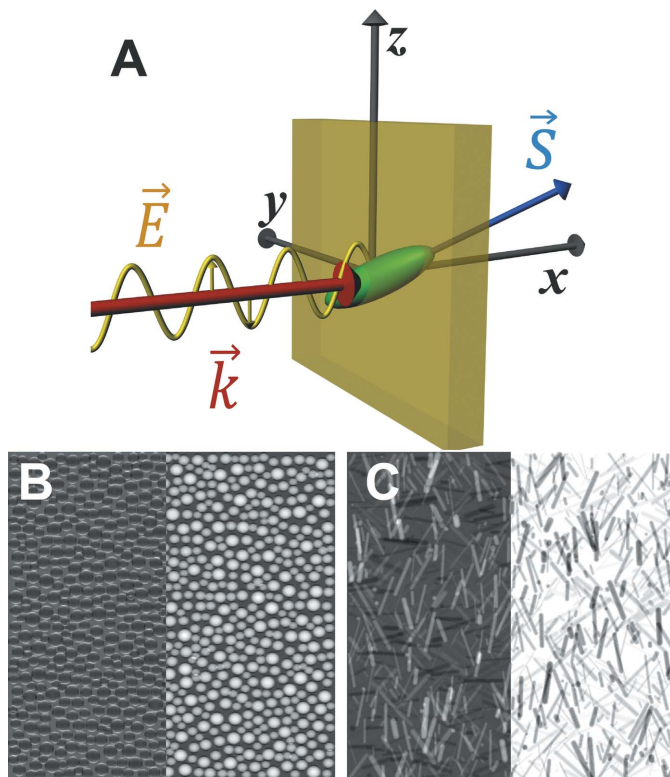


Figure 3

(A) Schematic of X-rays with \vec{k} normal to the film and \vec{E} along the z -axis. Molecular alignment is shown as an ellipsoid elongated along \vec{s} . (B, C) Real space projections along x of the full scale simulation ($2560 \text{ nm} \times 2560 \text{ nm}$) imaginary part (left) and magnitude (right) of p_z , at 289 eV are shown in (B) for interface-alignment face-on to spherical dispersions and (C) for fibrillar alignment. It is worth noting that, although the orientation of the fibrils in (C) is random, the scattering is emphasized in both perpendicular and parallel orientations to the incident X-ray polarization, resulting in a non-isotropic optical representation.

$$p_z = \sum_i \frac{1}{4\pi} \left[\Phi_{ui} \left(\frac{n_{||i} + 2n_{\perp i}}{3} \right)^2 + n_{||i}^2 s_{zi}^2 + n_{\perp i}^2 (s_{xi}^2 + s_{yi}^2) - \Phi_i \right], \quad (4)$$

and the depolarized components (which in non-polarized scattering classically do not contribute) are

$$\begin{aligned} p_y &= \sum_i \left(\frac{n_{\perp i}^2 - n_{||i}^2}{4\pi} \right) s_{zi} s_{yi}, \\ p_x &= \sum_i \left(\frac{n_{\perp i}^2 - n_{||i}^2}{4\pi} \right) s_{zi} s_{xi}. \end{aligned} \quad (5)$$

Note that \vec{p} reduces to the normal (unpolarized) term

$$\sum_i \frac{\Phi_i}{4\pi} (1 - n_i^2) \hat{z}$$

when the material is either isotropic on the molecular scale such that the parallel and perpendicular indices are the same ($n_{||i} = n_{\perp i} = n_i$) or is packed isotropically such that there is no preferential alignment ($\vec{s}_i = 0$), the unaligned component is the same as the material concentration ($\Phi_{ui} = \Phi_i$), and the index

of refraction reduces to the unaligned average [$n^2 \equiv \langle \hat{n} \rangle^2 = (n_{||}^2 + 2n_{\perp}^2)/3$]. Components of the induced molecular polarization (\vec{p}) orthogonal to the incident X-ray polarization (\vec{E}) (p_x and p_y in this geometry where we have set up the incident field to be along the z -axis) contribute when \vec{s} is non-zero in both x or y , respectively, and the excited direction (z). It is important to remember that \vec{s} , Φ and \hat{n} are attributes of the morphology, independent of the incident X-ray properties \vec{E} and λ , while \vec{p} , being the induced molecular polarization, varies with both the incident field and wavelength. Examples of the projection of the imaginary component and magnitude of p_z at 289 eV are shown in Figs. 3(b) and 3(c).

We use the Born approximation to calculate the far-field spherical electric field \vec{E}_s at location \vec{r} by taking the perpendicular (non-radial) projection of \vec{p} [as calculated in equations (4) and (5) above] Fourier transformed into \vec{q} space [denoted by $\tilde{\vec{p}}(\vec{q})$] as r goes to infinity,

$$\lim_{r \rightarrow \infty} \vec{E}_s(\vec{r}) = \frac{\exp(i\vec{k} \cdot \vec{r})}{|\vec{r}|} k^2 (\vec{I} - \hat{\vec{r}}\hat{\vec{r}}) \cdot \tilde{\vec{p}}(\vec{q}), \quad (6)$$

where

$$\vec{r} \cong \vec{k}_{\text{out}} = \vec{k}_{\text{in}} - \vec{q} = (k - q_x)\hat{x} - q_y\hat{y} - q_z\hat{z} \quad (7)$$

and $|\vec{r}| \cong |\vec{k}_{\text{out}}| = k$, so

$$\begin{aligned} k^2(I - \hat{\vec{r}}\hat{\vec{r}}) &= k^2 I - \begin{pmatrix} k - q_x \\ -q_y \\ -q_z \end{pmatrix} \begin{pmatrix} k - q_x & -q_y & -q_z \end{pmatrix} \\ &= \begin{pmatrix} (2k - q_x)q_x & (k - q_x)q_y & (k - q_x)q_z \\ (k - q_x)q_y & k^2 - q_y^2 & -q_y q_z \\ (k - q_x)q_z & -q_y q_z & k^2 - q_z^2 \end{pmatrix}. \end{aligned} \quad (8)$$

The differential scattering cross section can be written as the limit of the intensity of \vec{E}_s in the far field, so by taking $\vec{r} \rightarrow \vec{k}_{\text{out}}$ [from (8)] and rewriting (5) completely in terms of the momentum transfer vector defined by $\vec{q} = \vec{k}_{\text{out}} - \vec{k}_{\text{in}}$ we obtain the result

$$\frac{d\sigma}{d\Omega} = \left| r \lim_{r \rightarrow \infty} \vec{E}_s(\vec{r}) \right|^2 / E_0^2 = \left| k^2(I - \hat{\vec{r}}\hat{\vec{r}}) \cdot \tilde{\vec{p}}(\vec{q}) \right|^2. \quad (9)$$

It is important to note that not just the induced molecular polarization \vec{p} must be considered in all three dimensions in PSoXS but the Born approximation itself becomes considerably more complicated, and all tensor components must be calculated for each scattering location.

In summary, the simulation is conducted by creating the scalar material composition Φ_i and vector preferential alignment \vec{s}_i in each material i which together form the MOCC (Fig. 1, color and lines, respectively). Then, using equations (4) and (5) for a given incident X-ray defined by \vec{E} , \vec{k}_{in} and λ , we calculate the induced molecular polarization \vec{p} at each point in space. We then Fourier transform \vec{p} , and use equation (9) to simulate the scattering at each (q_x, q_y) location on the detector.

2.6. Sample preparation

The blend film was spin cast from chlorobenzene solution containing 1:1 (by weight) blend ratios of P3HT (Rieke) and PC₆₁BM (99.5%, Nano-C) to make a ~150 nm film. The films were thermally annealed at 150°C for 20 min. PSoXS measurements were performed at beamline 11.0.1.2 (Gann *et al.*, 2012) at the Advanced Light Source, Lawrence Berkeley National Laboratory, Berkeley, CA, USA, following previously established protocols (Gann *et al.*, 2012; Collins *et al.*, 2012).

3. Results

Fig. 4 presents several example simulated scattering patterns as well as experimental scattering patterns from a P3HT:PCBM blend sample as used in photovoltaic applications at several X-ray energies. The speckled texture results

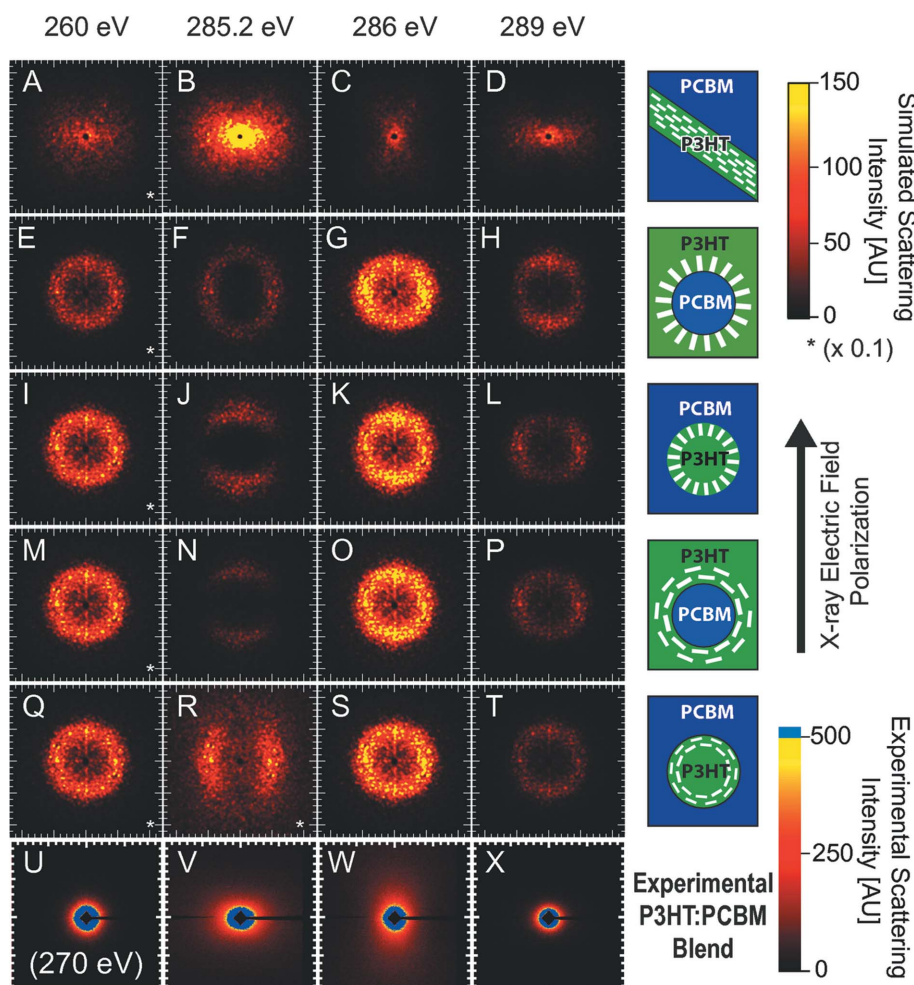


Figure 4

Simulated scattering patterns from the sample with alignment (*A–D*) within fibrils, (*E–H*) face-on to dispersions, (*I–L*) face-on within dispersions, (*M–P*) edge-on to dispersions, (*Q–T*) edge-on within dispersions at X-ray energies of (*A, E, I, M, Q*) 260 eV, (*B, F, J, N, R*) 285.2 eV, (*C, G, K, O, S*) 286 eV and (*D, H, L, P, T*) 289 eV. Experimental scattering patterns are shown for comparison at (*U*) 270 eV, (*V*) 285.2 eV, (*W*) 286 eV and (*X*) 289 eV. The 260 eV simulations and (*R*) are multiplied by 10 to allow details to be visible. All scattering patterns, simulated and experimental, are shown with q_y (x-axis) and q_z (y-axis) each ranging from -1 nm^{-1} to 1 nm^{-1} .

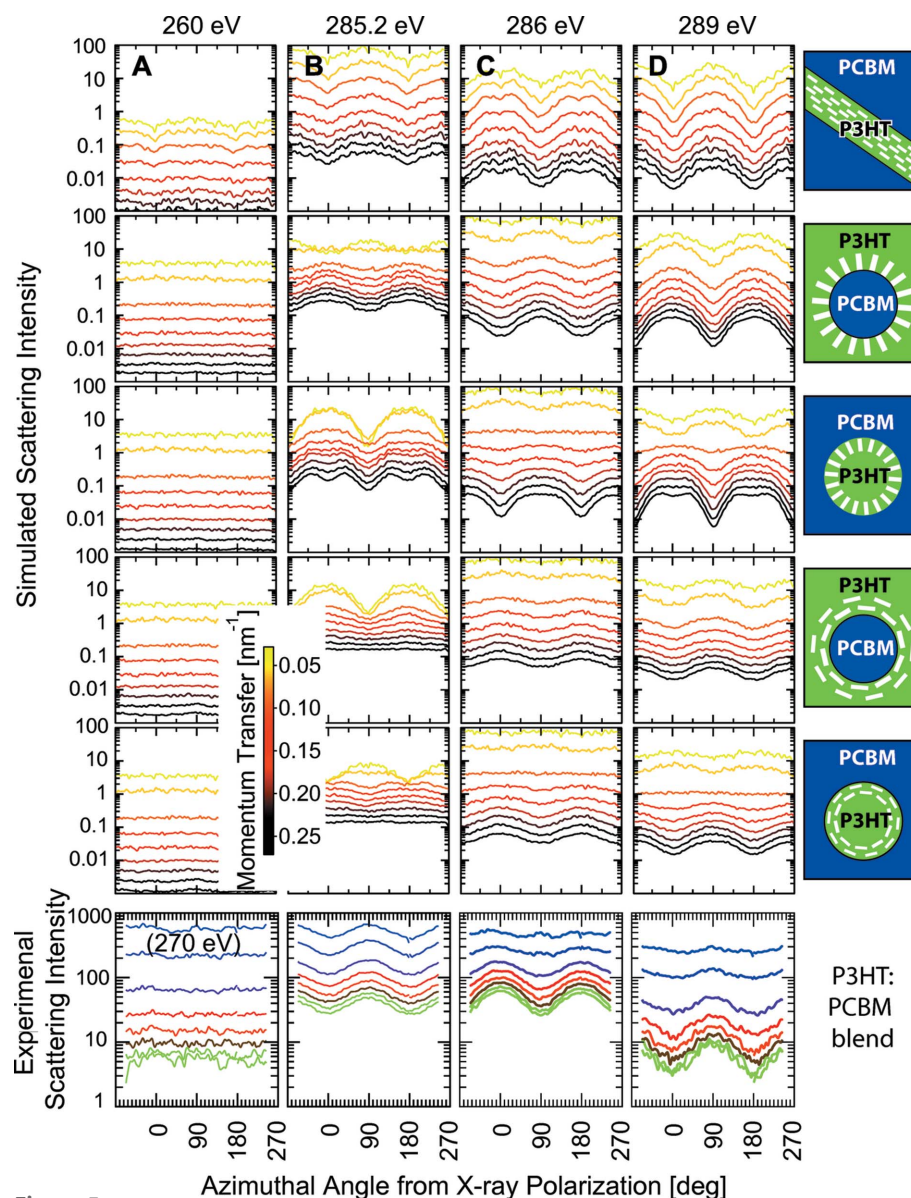
from the simulated perfectly coherent beam (Sinha *et al.*, 1998). Much of the speckle has been removed by applying a Gaussian filter with width of 0.01 nm^{-1} . This approximates the effects of a realistic beam size and level of coherence. A beamstop is simulated which blocks the scatter at $q < 0.01 \text{ nm}^{-1}$, a conservative estimate of the range of scatter currently obtainable in a single exposure (Gann *et al.*, 2012). This can also be seen by comparison with the experimental images, which cover the same q range.

The MOCCs simulated are themselves easily distinguished, because of the differing domain structure. Despite the similar size distributions of the domains, the fibrils have a long axis which contributes to scattering intensities at larger length scales (smaller q), so, whereas the spherical domains produce a ring of scattering intensity, the fibril-like domains, as well as the experimental blends, produce radially decreasing scattering patterns. It is tempting to initially compare the experimental blend scattering with that of the bulk-aligned fibril

MOCC, but at this point the comparison is dominated by the isotropic scattering intensity, which, rather than exhibiting a ring, has a uniformly decreasing signal with higher q . In a real system, this anisotropy, when added to an underlying isotropic scattering pattern from a different morphological feature, may appear differently, so such comparisons are discouraged, although in this instance they will prove to hold upon further analysis.

There is a clear similarity between these simulations [particularly scattering patterns such as Figs. 4(*J*) and 4(*L*)] and previously published ASPs of other systems (Collins *et al.*, 2012) in addition to the experimental scattering patterns of the P3HT:PCBM system. Several differences in anisotropy (particularly between the interfacial morphologies) are readily apparent in the two-dimensional scattering patterns, but, viewing only the two-dimensional scattering pattern, anisotropy only at the peak of isotropic intensity is readily apparent, so it is somewhat difficult to distinguish, for instance, alignment face-on to spherical dispersions from alignment edge-on within dispersions just by examining these two-dimensional scattering patterns. Details of PAXS, particularly the changes of anisotropy with q , and the amount of anisotropy at lower scattering intensities, cannot be gleaned by examining the data in this way.

To examine the ASPs in a form in which PAXS and isotropic intensity are on equal footing, Fig. 5 displays scat-

**Figure 5**

Azimuthal plots of scattering intensity at (A) 260 eV, (B) 285.2 eV, (C) 286 eV and (D) 289 eV. From top to bottom are simulations of morphologies shown in schematics (white lines represent the preferential direction of TDMs) to the right and in the bottom row are experimentally collected scattering. Experimental scattering in (A) is collected at 270 eV. Experimental signal to noise in a single exposure limits the azimuthal traces to be, from top to bottom, 0.01 nm^{-1} to 0.08 nm^{-1} , a smaller range than simulation allows.

tering intensity *versus* azimuth over a range of q and X-ray energies, along with experimentally collected ASPs from the P3HT:PCBM blend sample. PAXS is clearly a resonance phenomenon (Collins *et al.*, 2012; Tumbleston *et al.*, 2014), as oscillations vanish at X-ray energies far from the absorption edge (Fig. 5a). When interfacial alignment is inside the dispersed phase, PAXS at low q is 90° out of phase with that at higher q . Bulk fibrillar alignment shows nearly identical anisotropy at every q , although it changes dramatically with X-ray energy. Near the dominant π^* resonance at 285.2 eV, there is a contrast minimum between isotropic P3HT and PCBM. Here the majority of the simulated scattering arises

from the aligned portion of P3HT (refer to the optical constants and contrasts in Fig. 2). Although the scattering is not as intense as at other X-ray energies, intensity does not decrease as much with q , shown by the closely packed traces. Another interesting phenomenon occurs in the simulations of interfacial face-on dispersions, where the oscillations of the ASP change from having a wavelength of π to a clear $\pi/2$ component at higher q .

Experimentally collected data (bottom row of Fig. 5) are consistent with fibrillar bulk ordering. The overall phase behavior matches both bulk ordering and edge-on alignment; however, the lack of a change in phase with q more closely matches bulk alignment, agreeing with the general isotropic scattering shape as observed in Fig. 4. This result is expected, as it has been previously established that this particular system largely consists of P3HT fibrils (Kozub *et al.*, 2011; Savenije *et al.*, 2006), which agrees very well with our observation. We have confirmed that the molecular alignment within these P3HT fibrils is $\pi-\pi$ stacking along the length of the fibril, which could not be directly measured in a blend system before. Unfortunately, the limited q range for experimental values is due to geometrical limitations of a single exposure, but despite this limitation the identification of the fibrillar morphology is straightforward.

To examine the ASP quantitatively and systematically for each MOCC and many X-ray energies, we calculate a reduced PAXS ratio A from 20° sector averages of the ASP parallel and perpendicular to incident X-ray polarization,

$$A(q, \lambda, \hat{E}) = \frac{I_{\perp}(q, \lambda, \hat{E}) - I_{\parallel}(q, \lambda, \hat{E})}{I_{\perp}(q, \lambda, \hat{E}) + I_{\parallel}(q, \lambda, \hat{E})}. \quad (10)$$

Note that because $I \geq 0$, then $-1 \leq A \leq 1$. Equation (10) defines A in a similar manner to the anisotropic signal in a previous experimental report (Tumbleston *et al.*, 2014). $A = 0$ indicates isotropic signal, while deviations towards ± 1 indicate anisotropy perpendicular or parallel to the incident X-ray polarization, respectively. 20° sectors miss some information shown in Fig. 5, particularly the oscillations with wavelengths of $\pi/2$, but simplify the majority of ASPs for quick computation and comparison.

The energy and q dependence of A (Fig. 6) is unique for each MOCC. $A(q)$ exhibits a flipping of sign at almost all energies for morphologies with interfacial alignment in a dispersed phase [Figs. 6(B) and 6(E)]. When interfacial alignment is in the matrix phase [Figs. 6(A) and 6(D)], sign flips only occur when the X-ray energy is either below (face-on orientation) or above (edge-on orientation) 287 eV but not both. It is notable that $A(q)$ never flips sign in bulk alignment, consistent with the experimental data shown in Figs. 4 and 5, possibly a result of there being no fixed length scale between perpendicular and parallel alignment unlike the matrix-dispersion morphologies. Fig. 6(F) additionally shows fibrillar P3HT in a disordered (isotropic) P3HT matrix, in which all scattering must arise from the MOCC. Unlike all of the other patterns, $A(hc/\lambda)$ is constant, because the relative relationship between optical constants is unchanging. In experiments,

density differences between the crystalline and amorphous phases may obscure this effect, but we find it an interesting result of this simulation, revealing PAXS as a fundamentally independent morphological measure from isotropic intensity, while in an experiment the two are intimately tied.

4. Discussion

We simulate experimentally accessible scattering angles between 0.3° and 45° , corresponding to length scales from approximately 6.3 nm to 630 nm. For future experiments, it is encouraging that at 285.2 eV the lowest intensity scatter is within two orders of magnitude of the peak intensity, and so well within the experimental reach of modern in-vacuum detectors, with only geometric tiling needed to capture the entire simulated range of data. By using variable polarization

of the incident X-rays available from elliptically polarizing undulator-based synchrotron soft X-ray sources (Gann *et al.*, 2012), at a minimum, the sign of A should be straightforward to deduce from even quite noisy scattering data. Binarizing Fig. 6 into regions of two pure colors (or perhaps three with values experimentally indistinguishable from 0 being a third color) would remove little of the richness of the data. Indeed, distinguishing between the different morphologies would be no more difficult. In this way PAXS could identify both the orientational and compositional distribution, even when the measured intensity is quite noisy.

Although small-angle scattering is typically seen as a bulk measurement, molecular alignment occurring within a few nanometers of an interface can be apparent even far from the corresponding $2\pi/q$ size scale as shown by our simulations. This indicates that PAXS may enable unprecedented sensitivity to ordering at interfaces, in particular non-planar buried interfaces. A quantitative analysis of anisotropy may allow determination of the degree and width of these aligned regions.

Accurate optical constants are required to predict the particular anisotropic scattering behavior at particular X-ray wavelengths. Such optical constants for common materials are readily available (Dhez *et al.*, 2003; Watts *et al.*, 2011) and straightforward to measure (Yan *et al.*, 2013). Our presented framework [equations (3), (4) and (6)] will allow simulations of many additional MOCCs than presented here.

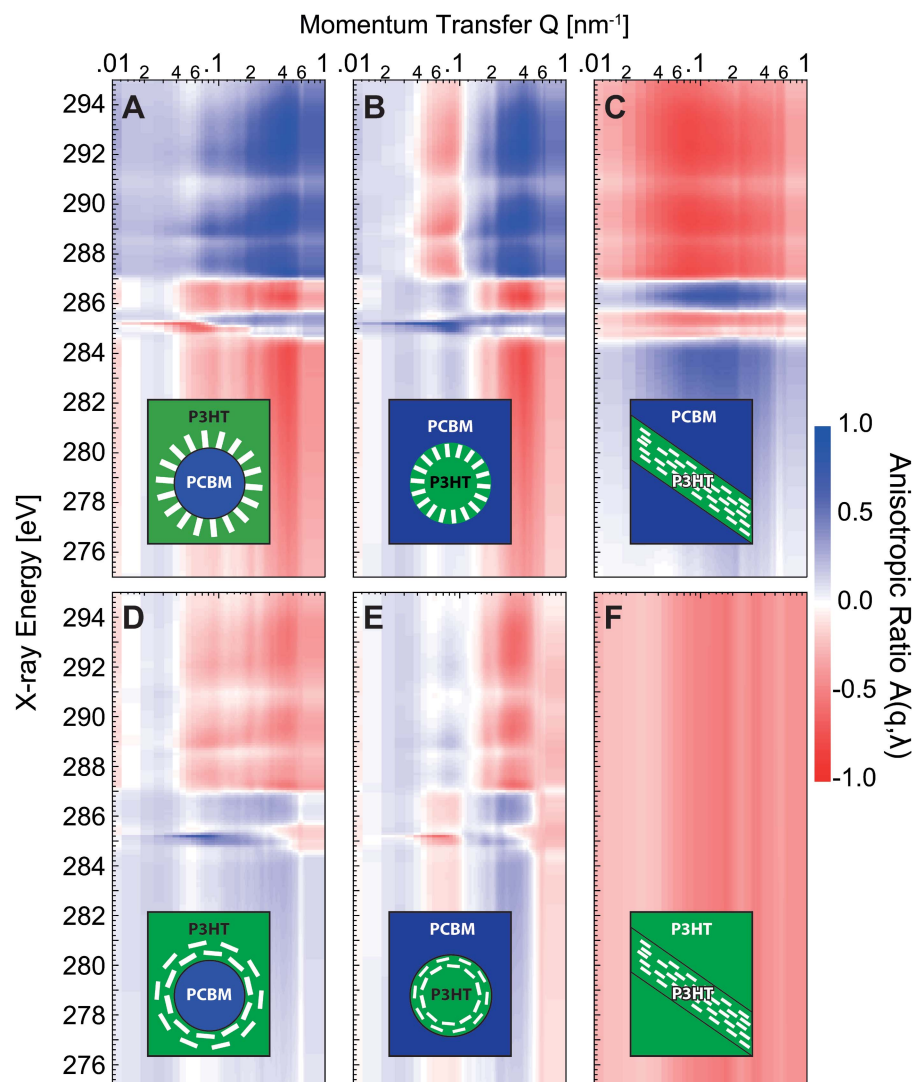


Figure 6

Reduced PAXS anisotropic ratio versus Q and X-ray energy (hc/λ) of (A) alignment face-on to spherical dispersions, (B) alignment face-on within spherical dispersions, (C) fibrils of P3HT in a P3HT PCBM mixed phase, (D) alignment edge-on to spherical dispersions, (E) alignment edge-on within spherical dispersions, (F) fibrils of P3HT in matrix of P3HT. Inset schematics show the morphologies graphically, where white lines indicate TDM alignment.

Further exploration of PAXS within more complex systems, including those modeled on spinodal decomposition, bulk heterojunctions, fibrils in which the long axis is along a different stacking direction, and combinations of these and other morphologies, are expected to result in a rich set of simulated scattering patterns for comparison with complex experimental data. Information from various microscopies and scattering techniques should be used to develop and refine morphological models when possible. The combined data from complementary experiments and simulations can result in a unique solution of both composition and alignment for myriad systems.

5. Conclusion

We have simulated and characterized ASPs resulting from bulk and various interfacial MOCCs, and compared these simulations with experimental results. Analysis of PAXS allows determination of local molecular alignment otherwise difficult to measure with other techniques, which lack either sensitivity to the molecular orientation or incident X-ray polarization control. PAXS produces a rich variety of anisotropic scattering that can, with this model, be used to definitively distinguish between types of alignment, allowing new insight into critical interfacial structure and ordering within otherwise largely disordered films.

Acknowledgements

Jongkuk Ko and Kookheon Char of Seoul National University provided the P3HT:PCBM blend samples. X-ray characterization by NCSU was supported by the NSF DMR-120-7032. X-ray data were acquired with the assistance of C. Wang and A. Young at beamline 11.0.1.2 (Gann *et al.*, 2012) at the Advanced Light Source, supported by US DOE DE-AC02-05CH11231.

References

- Albrecht, S., Vandewal, K., Tumbleston, J. R., Fischer, F. S. U., Douglas, J. D., Fréchet, J. M. J., Ludwigs, S., Ade, H., Salleo, A. & Neher, D. (2014). *Adv. Mater.* **26**, 2533–2539.
- Born, M. & Wolf, E. (1980). *Principles of Optics: Electromagnetic Theory of Propagation, Interference and Diffraction of Light*. New York: Pergamon Press.
- Brady, M. A., Su, G. M. & Chabiny, M. L. (2011). *Soft Matter*, **7**, 11065.
- Chen, D., Liu, F., Wang, C., Nakahara, A. & Russell, T. P. (2011). *Nano Lett.* **11**, 2071–2078.
- Collins, B. A., Cochran, J. E., Yan, H., Gann, E., Hub, C., Fink, R., Wang, C., Schuettfort, T., McNeill, C. R., Chabiny, M. L. & Ade, H. (2012). *Nat. Mater.* **11**, 536–543.
- Collins, B. A., Gann, E., Guignard, L., He, X., McNeill, C. R. & Ade, H. (2010). *J. Phys. Chem. Lett.* **1**, 3160–3166.
- Collins, B. A., Li, Z., McNeill, C. R. & Ade, H. (2011). *Macromolecules*, **44**, 9747–9751.
- Collins, B. A., Tumbleston, J. R. & Ade, H. (2011). *J. Phys. Chem. Lett.* **2**, 3135–3145.
- Dhez, O., Ade, H. & Urquhart, S. G. (2003). *J. Electron Spectrosc. Relat. Phenom.* **128**, 85–96.
- Diao, Y., Zhou, Y., Kurosawa, T., Shaw, L., Wang, C., Park, S., Guo, Y., Reinschach, J. A., Gu, K., Gu, X., Tee, B. C. K., Pang, C., Yan, H., Zhao, D., Toney, M. F., Mannsfeld, S. C. B. & Bao, Z. (2015). *Nat. Commun.* **6**, 7955.
- Gadisa, A., Tumbleston, J. R., Ko, D.-H., Aryal, M., Lopez, R. & Samulski, E. T. (2012). *Thin Solid Films*, **520**, 5466–5471.
- Gann, E., Young, A. T., Collins, B. A., Yan, H., Nasiatka, J., Padmore, H. A., Ade, H., Hexemer, A. & Wang, C. (2012). *Rev. Sci. Instrum.* **83**, 045110.
- Godbout, N., Salahub, D. R., Andzelm, J. & Wimmer, E. (1992). *Can. J. Chem.* **70**, 560–571.
- Goddard, W. A. (1992). *Abstr. Pap. Am. Chem. Soc.* **203**, 14-Catl.
- He, X., Collins, B. A., Watts, B., Ade, H. & McNeill, C. R. (2012). *Small*, **8**, 1920–1927.
- Hermann, K., Petterson, L. G. M., Casida, M. E., Daul, C., Goursot, A., Koester, A., Proynov, E., St-Amant, A. & Salahub, D. R. Contributing authors: Carravetta, V., Duarte, H., Friedrich, C., Godbout, N., Guan, J., Jamorski, C., Leboeuf, M., Leetmaa, M., Nyberg, M., Patchkovskii, S., Pedocchi, L., Sim, F., Triguero, L. & Vela, A. (2007). *StoBe-deMon*, Version 3.0, <http://www.fhi-berlin.mpg.de/KHsoftware/StoBe/index.html>
- Huzinaga, S. (1965). *J. Chem. Phys.* **42**, 1293.
- Kozub, D. R., Vakhshouri, K., Orme, L. M., Wang, C., Hexemer, A. & Gomez, E. D. (2011). *Macromolecules*, **44**, 5722–5726.
- Li, W., Yang, L., Tumbleston, J. R., Yan, L., Ade, H. & You, W. (2014). *Adv. Mater.* **26**, 4456–4462.
- Liu, F., Wang, C., Baral, J. K., Zhang, L., Watkins, J. J., Briseno, A. L. & Russell, T. P. (2013). *J. Am. Chem. Soc.* **135**, 19248–19259.
- Ma, W., Reinschach, J., Zhou, Y., Diao, Y., McAfee, T., Mannsfeld, S. C. B., Bao, Z. & Ade, H. (2015). *Adv. Funct. Mater.* **25**, 3131–3137.
- Ma, W., Tumbleston, J. R., Wang, M., Gann, E., Huang, F. & Ade, H. (2013). *Adv. Energ. Mater.* **3**, 864–872.
- O'Connor, B., Kline, R. J., Conrad, B. R., Richter, L. J., Gundlach, D., Toney, M. F. & DeLongchamp, D. M. (2011). *Adv. Funct. Mater.* **21**, 3697–3705.
- Pasquali, L., Terzi, F., Seeber, R., Doyle, B. P. & Nannarone, S. (2008). *J. Chem. Phys.* **128**, 134711.
- Savenije, T. J., Kroese, J. E., Yang, X. & Loos, J. (2006). *Thin Solid Films*, **511–512**, 2–6.
- Schuettfort, T., Watts, B., Thomsen, L., Lee, M., Sirringhaus, H. & McNeill, C. R. (2012). *ACS Nano*, **6**, 1849–1864.
- Singh, K. A., Young, T., McCullough, R. D., Kowalewski, T. & Porter, L. M. (2010). *Adv. Funct. Mater.* **20**, 2216–2221.
- Sinha, S. K., Tolan, M. & Gibaud, A. (1998). *Phys. Rev. B*, **57**, 2740–2758.
- Sirringhaus, H., Wilson, R. J., Friend, R. H., Inbasekaran, M., Wu, W., Woo, E. P., Grell, M. & Bradley, D. D. C. (2000). *Appl. Phys. Lett.* **77**, 406.
- Slater, J. C. (1972). *Advances in Quantum Chemistry*. New York: Academic Press.
- Tang, Y. & McNeill, C. R. (2013). *J. Polym. Sci. B*, **51**, 403–409.
- Tumbleston, J. R., Collins, B. A., Yang, L., Stuart, A. C., Gann, E., Ma, W., You, W. & Ade, H. (2014). *Nat. Photon.* **8**, 385–391.
- Wang, C. H., Mukherjee, S., Maidul Islam, A. K. M., Yang, Y. W. & Mukherjee, M. (2011). *Macromolecules*, **44**, 5750–5757.
- Watts, B. (2014). *Opt. Express*, **22**, 23628–23639.
- Watts, B., Swaraj, S., Nordlund, D., Lüning, J. & Ade, H. (2011). *J. Chem. Phys.* **134**, 024702.
- Yan, H., Wang, C., McCarn, A. R. & Ade, H. (2013). *Phys. Rev. Lett.* **110**, 177401.